COMPARISON OF PRESTACK STEREOTOMOGRAPHY AND NIP-WAVE TOMOGRAPHY FOR VELOCITY MODEL BUILDING: INSTANCES FROM THE MESSINIAN EVAPORITES

K. Meier, S. Dümmong, D. Gajewski and C. Hübscher

email: *kristina.meier@zmaw.de*

keywords: *Velocity model building, tomography*

ABSTRACT

Velocity model determination during seismic data processing is crucial for any kind of depth imaging. We compare two approaches of grid tomography: prestack stereotomography (PST) and NIP-wave tomography (NIPT). Whereas NIPT is based on wavefield attributes obtained during the CRS stack, and thus on the underlying hyperbolic second-order traveltime approximation, PST describes traveltimes by local slopes (i.e. linearly) in the prestack data domain. To analyze the impact of the different traveltime approximations and the different input data domains on velocity model building we have applied both techniques to two profiles of a real marine data-set from the Levantine Basin/ eastern Mediterranean. Owing to the presence of a thick tabular mobile unit of the Messinian evaporites strong vertical and lateral velocity contrasts have been expected. The obtained velocity models reveal that the reconstruction of high velocity contrasts by grid tomographic methods is limited due to the smooth description of the velocity distribution. The lateral resolution of velocities obtained from PST appears to be better than those from NIPT which is related to the difference in the approximation of traveltimes, the determination of input data, and the description of the velocity distribution. Other differences are mainly caused by different implementations of the inversion schemes and outliers in the input data. Nevertheless both algorithms provide suitable models for a further residual move-out analysis.

INTRODUCTION

For the transformation of the recorded seismic data to the desired depth section, a correct migration velocity model is always required. Different approaches for velocity model estimation were proposed in the past. They can be mainly divided into two groups: migration-based methods and tomographic methods. Two of these methods belonging to the second group are NIP-wave tomography by Duveneck (2004) and prestack stereotomography by Billette and Lambaré (1998).

NIP-wave tomography depends on wavefield attributes resulting from the CRS stack e.g. Mann (2002), and therefore based on a hyperbolic second-order traveltime approximation. The parameters used for velocity model estimation are the second derivatives of the traveltime (wavefront curvatures), the angle of emergence, the one-way traveltime, and the lateral positions picked from the CRS stack attribute sections. Picking of these attributes is facilitated in the CRS domain/ poststack data domain with its high signal to noise ratio. In NIP-wave tomography, the extracted wavefield parameters do not need to belong to a consistent event.

In stereotomography, reflection traveltimes are approximated by local slopes which are directly linked to the horizontal component of the slowness vector. These slopes, their related traveltimes and spatial positions at the surface are used for the estimation of a smooth velocity model. They are obtained in the prestack data domain by automated picking. Since only locally coherent events are considered no

assumptions on the lateral heterogeneity of the velocity distribution nor the continuity of any interfaces are made.
Both methods are based on a grid tomographic approach, therefore leading to a smooth velocity model. Unlike in conventional horizon based schemes no interpretation of events is necessary; however, the vertical resolution of structural boundaries is limited by the grid size and the description of the velocity model. In this article, we compare the two presented methods to analyze the impact of the differences in their formulation on velocity model building. We have applied both techniques to two profiles of a real marine data-set from the Levantine Basin /eastern Mediterranean. Owing to the presence of thick tabular Messinian evaporites strong vertical and lateral velocity contrasts (> 2000m/s) have been expected.

THEORETICAL BACKGROUND

NIP-wave tomography

NIP-wave tomography (Duveneck and Hubral, 2002; Duveneck, 2004) uses the concept of focusing a NIP-wavefront back to its hypothetical sourceŠ (Hubral and Krey, 1980) which is related to the principle of depth focusing analysis in the determination of migration velocities (MacKay and Abma, 1992).
The NIP-wave is a hypothetical wave which starts at the Normal Incidence Point (NIP) of a reflector in depth and arrives with a certain angle at the corresponding Zero Offset position at the surface. Thus the NIP-waves are linked to a certain points in the subsurface for a given velocity model. All NIP-waves focus at zero time if the velocity model is consistent with the data.

The input data for NIP-wave tomography are obtained from the CRS stack and the accompanying attribute sections (wavefield attributes). The CRS stack is a multiparameter stacking method based on a hyperbolic second-order traveltime approximation in offset and CMP cordinates. The wavefield attributes are also referred to as CRS parameters. They are used to estimate a smooth velocity distribution.
Since NIP-wave tomography is based on a second order approximation of the traveltimes the algorithm is limited to regions with moderate lateral velocity variations. However, the advantage of estimating all parameters in the CRS stacked sections with a high signal to noise ratio significantly simplifies the picking of the attributes. Therefore, NIP-wave tomography is applicable to data with low signal to noise ratio.

The inversion problem for the 2D case can be formulated in the following way: the emerging NIP-wavefront is characterized by four parameters, the traveltime of the normal ray τ the corresponding coordinate at the surface x, the horizontal slowness component p, and the second spatial derivative of the traveltime M_{NIP}. Consequently, an emerging NIP-wave can be characterized by the data point (τ, M_{NIP}, p, x). The true subsurface locations (X, Z) and the local dips α, defining the normal ray direction, are initially unknown. They are determined during the inversion process along with the smooth velocity distribution which is described by B-splines in the order of four. This order is required, since the Fréchet derivatives of the ray-tracing operator require continuous third derivatives of the velocity field. The subsurface model description is given by (X, Z, v_{ij}), where v_{ij} denotes the B-spline coefficients. The velocity distribution is determined in the following way: dynamic ray tracing is performed starting at the considered grid point in depth. By minimizing the misfit between the modeled data and the data points extracted from the CRS stack in a least square sense, the algorithm determines the velocity model that fits the data best. The inversion problem is solved by a conjugate gradient like scheme (LSQR) (Paige and Saunders, 1982).

Prestack stereotomography

Prestack stereotomography was proposed, developed, and applied by Billette and Lambaré (1998). It uses additionally slope information to invert the data and is based on the concept of locally coherent events. These are seismic events which have to be tracked only over a limited number of traces around a central trace. In stereotomography, the attributes of these events are used for the estimation of a smooth velocity macro-model.

Seismic events are characterized by the position of their central trace, i.e. its associated source and receiver position (S, R) by their central two-way traveltime T_{SR} and by their local slopes (p_R, p_S) i.e., the tangents on the traveltime curves at the central trace in a common-shot and a common-receiver-gather. Since only locally-coherent events are considered, each set of parameters (S, R, p_S, p_R, T_{SR}) provides information on the velocity model independently of all other events. Consequently, no assumptions on interfaces nor on the velocity distribution are necessary.
As in all slope tomographic methods, in addition to traveltime information, the slopes constrain the velocity model as they are directly linked to the horizontal component of the slowness vector. Each event corresponds to a pair of ray segments from a reflection/diffraction point X in the subsurface to either the source or the receiver. Each ray segment is completely defined by its start and end point, its angle of emergence or incidence (θ_S, θ_R), and the associated one-way traveltime (T_S, T_R) to the source and receiver, respectively. In the case of a correct velocity model, both segments will satisfy the following boundary conditions: they must join each other i.e., terminate at the same reflection/diffraction point in depth and they must explain the positions, slopes and two-way traveltimes of the event at the surface.
If the velocity model is incorrect, these conditions cannot be satisfied by both ray segments simultaneously. This means that at least one of the boundary conditions has to be ŠrelaxedŠ. This principle is used by stereotomography: the difference between the parameters describing the relaxed boundary condition and the ideal situation (i.e. a pair of ray segments in the correct model) is used to constrain the velocity model. Based on this, an inverse problem is constructed in which the model space is described by the velocity field and a group of ray segment pairs.

In practice, the boundary condition at the surface is relaxed (become variable) and a cost function containing the misfits in source and receiver positions, associated slopes and traveltimes is evaluated. The data measured at the surface are fitted in a least-square sense to data modeled by raytracing which is performed in a smooth velocity model described by cardinal cubic B-splines. Thus, the model space in stereotomography is composed of a discrete description of the velocity field denoted by B-spline coefficients v_{ij}, a group of reflecting/diffracting points, two angles of emergence and two one-way traveltimes. These parameters are updated by a joint inversion until they explain each data point $(S, R, p_S, p_R, T_{SR})_n$ within prescribed error margins. For inversion a conjugate gradient like method called LSQR (Paige and Saunders, 1982) is used.

DATA EXAMPLES

Geological setting

The data set from the central Levantine Basin/ Eastern Mediterranean covers the basinal succession or mobile unit (MU) of the Messinian Evaporites, the Pliocene-Quaternary overburden, and the upper pre-Messinian succession (Fig 1). 2D acquisition was performed, with a shot spacing of 25 m and a receiver spacing of 12.5 m, with maximum offsets of 7325 m. According to the chronostratigraphic scheme of Clauzon et al. (1996) or Krijgsman et al. (1999) the precipitation of the MU started around 5.6Ma during the Messinian Salinity Crisis (MSC). The end of the MU formation and the rapidity with which the Mediterranean basin was refilled at the end of the MSC - between a few thousand years (Clauzon et al., 1996) and about 200000 years (Krijgsman et al., 1999) - are still a matter of debate. In the following and according to Ryan et al. (1970), the base of the Pliocene-Quaternary succession will be called the M-reflection and the base of the MU the N-reflection.
Recent publications showed a complex seismic stratigraphy of the MU in the Levantine Basin (Gradmann et al., 2005; Netzeband et al., 2006a; Bertoni and Cartwright, 2006), which can be divided into six sequences (Hübscher et al., 2007; Hübscher and Netzeband, 2007). Sequences ME-I, II, IV are seismically transparent and sequences ME-III and ME-V reveal several internal and subparallel reflections (Hübscher and Netzeband, 2007). The absence of seismic reflections is typical of salt bodies (Mitchum et al., 1977) and so the internal velocity is expected higher than 4km/s (Netzeband et al., 2006a). The internal reflections habe been interpreted as intercalated (and presumably overpressurized) clastics by Garfunkel et al. (1979) and Gradmann et al. (2005). However, 3D-seismic data analysis proved a high lateral continuity of seismic reflection characters and identified polarity changes which are more indicative of chemical sedimentation

processes (Bertoni and Cartwright, 2007).

The deformation pattern of the intra-evaporitic sequences include folds and thrust faulting, which gives evidence for extensive salt tectonics and shortening, respectively, during the depositional phase. Both, the identified evaporitic facies of the individual intra-evaporitic sequences and the driving forces for the syn-depositional shortening remain unclear. Post-depositional gravity gliding caused salt rollers in the extensional marginal domain, compressional folds, and faults within the Levante basin (Gradmann et al., 2005; Hübscher and Netzeband, 2007).

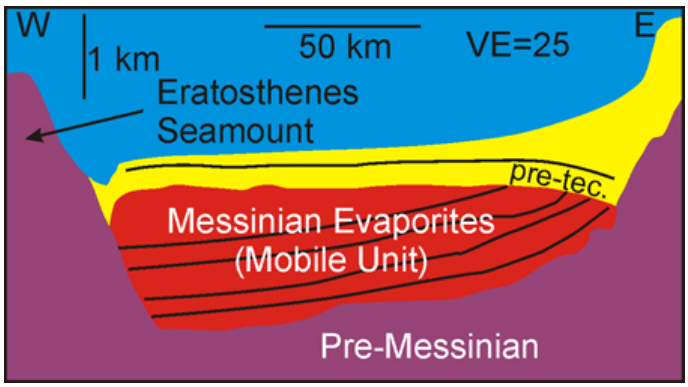

Figure 1: Linedrawing of depth migrated seismic section from the Levantine Basin/Eastern Mediterranean (after Hübscher and Netzeband (2007)). Up to 2km thick Messinian evaporites are covered by Pliocene-Quaternary succession.

Velocity model building and depth-migration in salt bearing basins is a challenging task for several reasons. The vertical velocity contrast between the MU and the overburden is bigger than 2 km/s, since interval-velocities of $4.3 - 4.4$ km/s were determined for the evaporites and $1.7 - 2.1$ km/s for the overburden, respectively (Netzeband et al., 2006b). If the MU are folded, strong lateral velocity contrasts occur at their top. Small thickness undulations of the MU cause apparent reflection undulations beneath (velocity pull-ups/-downs), which may be spuriously interpreted as folds or faults. The intra-evaporitic reflections reveal much weaker amplitudes than the top or base of the MU.
In the following we will present a comparison of the two tomographic methods on two data examples. One is a distal profile part, with a basically horizontally layered geological setting, dominated by a strong vertical velocity contrast between the sediments and the salt and a large fault structure in the salt. Here, the focus of the comparison is on vertical resolution of the velocity models. The second data example is a proximal profile part with a strong inhomogeneous geological setting. Typical salt roller structures occur where the salt body pinches out against the shelf. The strong lateral velocity variations allows the comparison of the lateral velocity resolution of both methods. The first example is located in the distal part of the profile from the coast and the second is located in the proximal part of the profile.

Distal data example

Description of the profile The first example covers 1000 CMP locations. The associated CRS stack section is displayed in Fig 2. Up to 2.7 s TWT the post-messinian sediments can be observed. The MU can be identified between 2.7 s and 3.5 s. The reflection at approximately 2.7 s corresponds to the top of salt reflection (M) and the reflection at 3.5 s to the bottom of salt (N). The internal reflection pattern of the MU can also be recognized. Below the N-reflection the pre-messinian sediments are visible. At position 122 km, a large fault structure can be identified, which pierces the sea floor. From the stacked section it remains unclear, wether the fault terminates at the base of the salt or it continues in depth.

This profile example is particularly suitable for investigating the vertical resolution of both tomographic methods. The methods have to deal with a strong velocity contrast between the sediments and the salt body. Furthermore the applicability in the vicinity of a large fault structure can be compared. The comparison

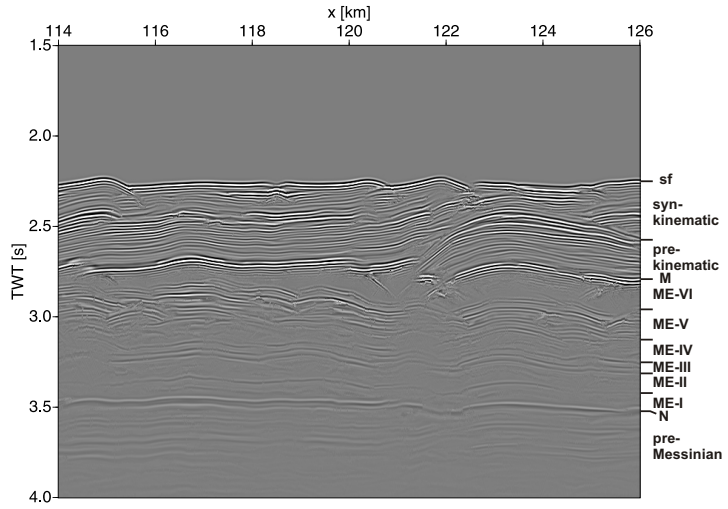

Figure 2: Distal data example. Between 2.7 s and 3.5 s the mobile unit (MU) of the Messinian evaporites can be identified. The Mu reveals six evaporitic sequences (Hübscher et al., 2007). The Pliocene-Quaternary overburden is subdivided into a pre- and synkinematic sequence.

should be drawn with special emphasizes to the data domain (where the input data for the inversion is generated) and the vertical resolution under equal initial conditions. The Common image gathers (CIGs) are used to evaluate the results. The same prestack depth migration tool was used for both methods.

Application of NIP-wave tomography To process the data example 2 with NIP-wave tomography we performed a CRS stack in order to acquire the necessary kinematic wavefield attributes. The CRS aperture was optimized to obtain reliable wavefield attributes for the automatic picking algorithm, which produces the input data of NIP-wave tomography. Furthermore an event consistent parameter smoothing (Hertweck et al., 2005) was applied to the wavefield attributes, to remove unphysical fluctuations in the data. We used an automatic picking tool for the input data extraction. This automatic picking tool identifies the events in the CRS attribute sections mainly on semblance criteria. Depending on a pre-defined threshold only the most reliable reflections are picked. After picking, quality control for the picks followed in order to remove outliers from the data. This quality control was mainly based on stacking velocities computed from picked CRS attributes and followed the practical aspects discussed in Duveneck (2004).
With the extracted and edited picks we performed NIP-wave tomography. We used the same initial velocity model $v(z) = 1500m/s + 0.4s^{-1}z$ as in prestack stereotomography. The initial B-spline spacing was directly chosen to 125 m vertically and 500 m laterally. This choice was possible due to the fact that NIP-wave tomography works in the poststack data domain i.e., less input data need to be inverted and the inversion process is more stable from the beginning. But nevertheless the inversion had to be stabilized in the water column and the corresponding B-spline nodes were fixed to water velocity. All input parameters were weighted equally during the inversion and after ten joint inversion iterations the cost function reached its minimum.
Fig 3(b) shows the result of NIP-wave tomography.The velocity distribution is displayed together with the locations of the modeled NIPs related to every input event. The position of the seafloor is clearly marked at a depth of 1700 m and a velocity increase to 3000 m/s represents the sedimentary overburden above the top of salt at 2200 m. The subsequent high velocity body incorporating zones ranging up to 4500 m/s, corresponds to the evaporites. The velocity inversion at a depth of about 3500 m describes the salt-sediment transition. The velocity distribution indicates the geologic structures in the depth migrated image, but here the data coverage was not satisfactory in the vicinity of the fault structure (122 km). As Fig 2 illustrates, in this area no reflections were present in the CRS stacked section and hence the estimation of reliable input parameters was not possible.

The resulting prestack depth migrated image using a Kirchhoff first arrival-maximum energy approach, and the corresponding CIGs are displayed in Figs 3(b) and 4, respectively. The quality of the depth migrated image is good, all sediments are imaged well over their entire tickness of 500 m. The M-reflection is imaged in a depth of 2200m. The salt body shows all internal features and the N-reflection is quite flat. The fault structure shows some significant velocity pull-up effects and has to be considered as unreliable, due to the poor input data illumination.

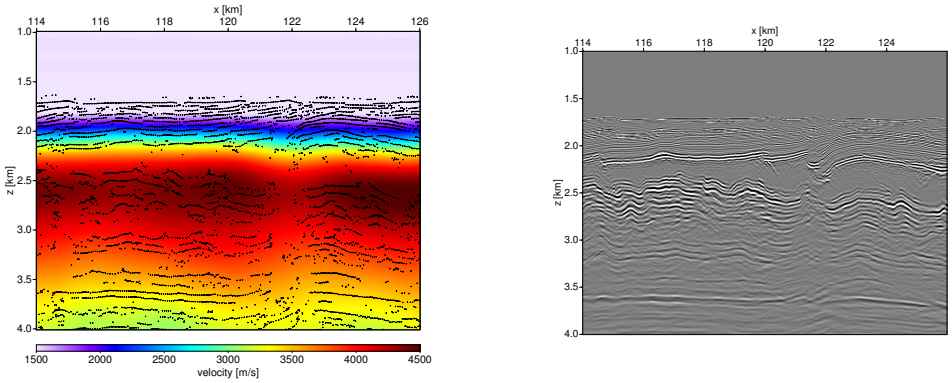

(a) NIP-wave tomography result. **(b)** Corresponding migrated section.

Figure 3: The result of NIP-wave tomography. The depth converted input data picks associated with the corresponding NIPs are imaged overlaid on the velocity distribution. On the right the corresponding prestack depth migration result.

Fig 4 shows selected CIGs equally spaced over the whole profile. All reflections are flattened quite good. Some residual move-out can be observed in the transition between the sediments and the salt body, were the smooth velocity description could not handle the strong velocity contrast. Nevertheless, NIP-wave tomography produced a velocity model consistent with the data.

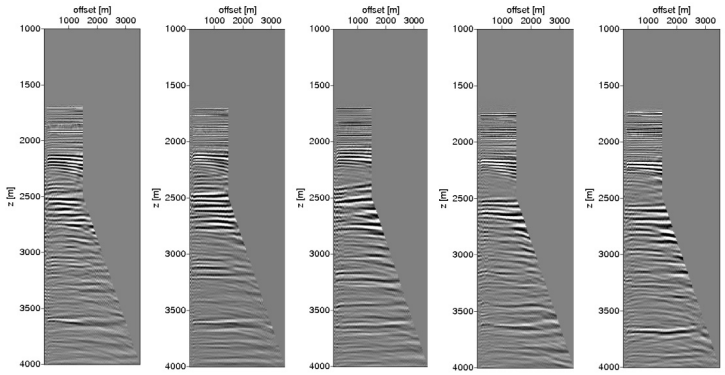

Figure 4: Selected common image gathers over the whole profile example.

Application of prestack stereotomography In order to perform prestack stereotomography additional preprocessing steps preceed the actual tomographic inversion. In the frame of this profile part the preprocessing consisted of multiple suppression via *f-k* filtering, a t^3-gain control to ensure the amplification of later events, and of applying a so called stereotomographic mute, to focus the automatic input data selection on the most relevant parts of the data and to avoid picking of refracted events.

After preprocessing, the semblance coefficient was estimated every 50 m using 8 traces for local slant stack calculation. The initial thresholds for a pick to be accepted were set to a minimum semblance of 0.6 in each common-shot and common-receiver gather, respectively, and events with an energy less than -40 dB from the highest energy observed for the current central trace were skipped.
After application of the automatic picking algorithm (Podvin, 2001), we applied a first quality control sequence for the input picks. It consisted of an interactive selection of picks. Due to strong energy differences in the data (i.e. reflections from the sediments and the salt) the input data was divided into three parts, discriminated by different traveltimes and energy thresholds. The first part mainly consisted of picks from the sediments, the second one of picks from the sediments and the upper parts of the MU body, and the last part mainly of picks from the MU. To further remove outliers in the data, each input data subset was inverted and a global normalized misfit quality control scheme was applied during the inversion. The first two data parts were inverted using a constant staring model of $v(z) = 1500\ m/s$ and the third one was inverted with a starting model of $v(z) = 1500\ m/s + 0.4s^1 z$. For each input data part first localization steps, where only the pairs of ray segments are optimized fixing the velocity model to its initial value, and afterwards joint inversions were performed. Due to the energy decrease in the data and increasing complexity different error thresholds and regularizations were used for this quality control.
After this quality control sequence, the inversion with the whole input data range was started again. This time a initial velocity function of $v(z) = 1500\ m/s + 0.4s^1 z$ was assumed and an initial B-spline grid of $500\ m * 500\ m$ was chosen. First, 10 localization steps preceded 10 joint inversion steps with a strong regularization, where already a significant decrease of the cost function could be observed. In order to increase the vertical resolution of the model we redefined the node spacing to 125 m in depth. To resume another 20 joint inversions with a loose regularization were performed. However, velocity model estimation was stopped after 17 iterations since no further decrease of the cost function was noted.
Fig 5(a) shows the result of prestack stereotomography. The high velocity area refers to the MU (starting at a depth of 2250 m). The strong gradient from $1550\ m/s$ to $3000\ m/s$ on top of the MU represents the post-messinian sediments. The depth converted input picks for the inversion are overlaid over the velocity distribution. In general a good data coverage could be achieved. Especially next to the fault structure (around 122 km), with its complicated reflection pattern and low coherency values, sufficient picks are available. No events from the pre-messinian sediments were estimated at the base and underneath the MU and therefore no velocity inversion is present, but this was not the aim of the processing.

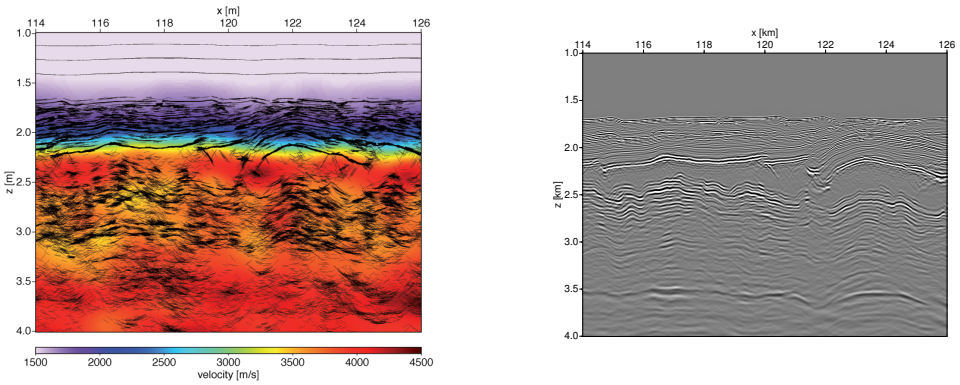

(a) Prestack stereotomography result.

(b) Corresponding migrated section.

Figure 5: The result of prestack stereotomograhy. On the left the velocity distribution. The depth converted input picks are displayed overlaid on the velocity model. On the right the corresponding prestack depth migration result.

On the right in Fig 5(b) the corresponding prestack depth migrated section is shown. A good image quality like in the result of NIP-wave tomography was obtained. The upper sequence of sediments is clearly imaged and the top of the evaporites is well-defined. The salt layer itself is about 1400 m thick and the intra-evaporitic sequences can be traced easily since they are continuous over the section. Beneath the

fault structure (position 122 km), the base of the evaporites is interrupted and downbended. However, this area is not reliably imaged due to the lack of input information describing the lower boundary of the salt. The derived velocities correlate quite well with the reflection characteristics of the particular Messinian sequences. The seismically transparent sequences ME-I, II, IV and VI reveal the highest velocities of up to 4.4km/s which corresponds to their interpretation as halite (Hübscher and Netzeband, 2007; Kearey and Brooks, 1991). The sequences ME-III and V which reveal the sub-parallel reflections are characterized by lower velocities which suggest the presence of, e.g., intercalacted clastics or evaporites facies with lower velocities like Gypsum.
Fig 6 presents selected Common-Image gathers (CIGs) which are equally spaced over the whole section. A maximum offset of 3500 m is shown. The good quality of the image is reflected in mainly flat gathers throughout the whole section. However, at a depth of about 2100 m some negative residual moveout remains. Here, the strong increase in velocity related to the sediment-salt transition cannot be described correctly by the underlying assumption of a smooth velocity model. Nevertheless, the events at the base of the evaporites are flattened quite well. We conclude that the estimation of a data consistent velocity model leading to flat image gathers was possible by prestack stereotomography.

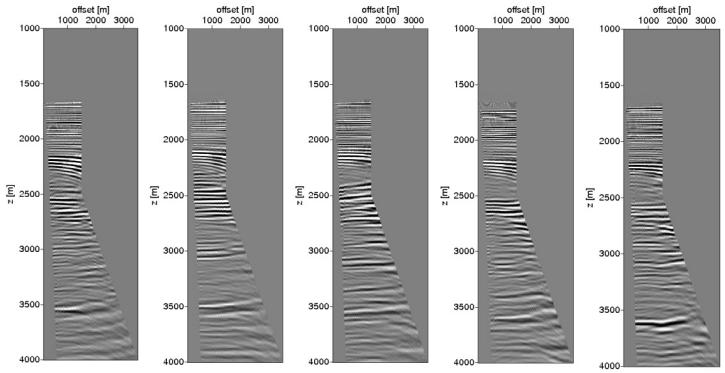

Figure 6: Selected common image gathers over the whole profile example.

Comparison of the results As demonstrated by this real data example, both tomographic approaches provide an velocity model with a different vertical resolution, nevertheless leading to a clear image in depth and mainly flat common-image gathers. However, despite of the high quality of the imaged sections, pronounced differences occur in the underlying velocity distributions. Whereas the velocity model obtained by NIP-wave tomography shows a smoother lateral and vertical variation and causes slight residual move-out in the vicinity of the fault system, the stereotomographic velocity distribution is more constrained in this area and presents a better lateral resolution.The derived velocities are more consistent with the geometry of the resolved stratigraphic layers and correspond to the internal reflection characteristic. These issues are directly linked to the approximation of the traveltime curves in the different approaches and the description via B-splines of different orders. In prestack stereotomography the traveltime is approximated by locally coherent events, i.e. linearly. In contrast to that, in NIP-wave tomography the traveltime curve is described by the second order hyperbolic traveltime approximation, i.e. a more regional approach. Furthermore prestack stereotomography uses one order lower B-splines. These two facts and the different regularization of the inverse problem explain the smoother image obtained by NIP-wave tomography.
The data coverage in prestack stereotomography is in general better than in NIP-wave tomography, especially near the fault system. This is due to fact that different data domains are used for input data generation. The poststack data domain leads to a reduced data volume, but has disadvantages near fault systems, were the coherency values of the CRS stack decrease significantly.
Generally higher average velocities are obtained by NIP-wave tomography over the whole profile part. This fact can be explained by the different regularization of both methods. Whereas in NIP-wave tomography the smoothest solution is explicitly sought by employing a minimum curvature constraint, in prestack

stereotomography the model vector is required to have a bound on its norm. Depending on the regularisation weight, this may influence the velocity distributions in terms of average velocities.

Proximal data example

Description of the profile The proximal profile example covers 1500 CMP locations. The associated CRS stack section is displayed in Fig 7. As the time section shows, the M-reflection can be identified at 2.7 s two-way traveltime in the left part of the section and at approximately 2.4 s in the right part. The subsequent layer of Messinian Evaporites covers only the seismically transparent sequences ME-I and III and can be observed only between position 145 km and 161 km. Salt roller structures can be found in form of triangular patterns. Again, below the N-reflection weaker reflections from pre-Messinian sediments can be recognised.

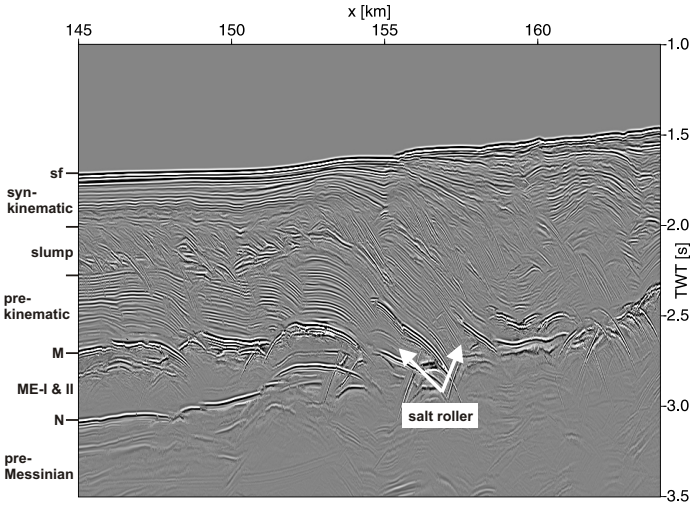

Figure 7: Proximal profile example. The MU pinch out to the right hand side of the section where salt rollers evolved. A slump subdivides the Pliocene-Quaternary overburden into a pre- and syn-kinematic succession (Netzeband et al., 2006b).

This data example is especially suitable for comparing both methods in an area with strong lateral velocity variations, which occur in the salt roller area. In this complex geologic setting the lateral resolution of both methods will be investigated and compared. Additionally, the quality of the resulting depth migrated images and the data domain for input data generation will be evaluated.

Application of NIP-wave tomography In order to obtain the necessary input data for NIP-wave tomography, we performed CRS stacking. The determination of the wavefield attributes had to be chosen carefully to ensure the most reliable results. Before picking of the attributes, the same preprocessing steps were performed as for the previous example. After application of the automated picking tool for extracting the input data for the inversion, a quality control sequence was applied. As before, the main criteria were stacking velocities and the position of picks.
To initialize the inversion we chose an initial B-spline node spacing of 500 m laterally and 125 m vertically and created an initial velocity model of $v(z) = 1500\ m/s + 0.5s^{-1}z$. During the inversion the B-spline nodes in the water column were fixed to water velocity. All input data picks were weighted equally. The inversion algorithm performed a total of 10 joint inversions, before it reached the minimum of the cost function.
The resulting velocity distribution is shown in Fig 8(a). As illustrated, the velocity distribution is linked to the structures in the model, but does not follow them explicitly. It is more smeared over the whole profile part. In some areas, the pick coverage is quite coarse and in the region between 156 km and 164 km the

N-reflection is not sufficiently described. The location of the seafloor is indicated by a smooth increase in velocity at depth ranging from 1100 m to 1300 m. A subsequent rise up to 1900 m/s corresponds to the layers above and the slump complex itself. In the following part, the velocity increases further quite evenly throughout the whole section and in the non-constraint regions it reflects given initial values. A large high-velocity zone between 145 km and 156 km comprising values up to 4000 m/s represents the evaporites with their base located slightly deeper than 3000 m.
To investigate the quality of the velocity model obtained by NIP-wave tomography, we carried out prestack depth migration, again. The resulting depth image is presented in Fig 8(b). A good image quality was achieved. The overburden of sediments is clearly imaged and its thickness ranges from approximately 700 m to 1000 m. Extensional faults can be traced and some faults pierce the sea-floor. Beneath the overburden, the top of the evaporites is well-defined and triangular patterns represent the salt roller structures. Maximum depth for the M reflection are 3000m. In the right part of the section the base of the evaporites is several times interrupted and shifted in depth. In the area around 148 km to 150km the M reflection seems continuous. Generally the image demonstrates smooth variations and continuous reflectors.

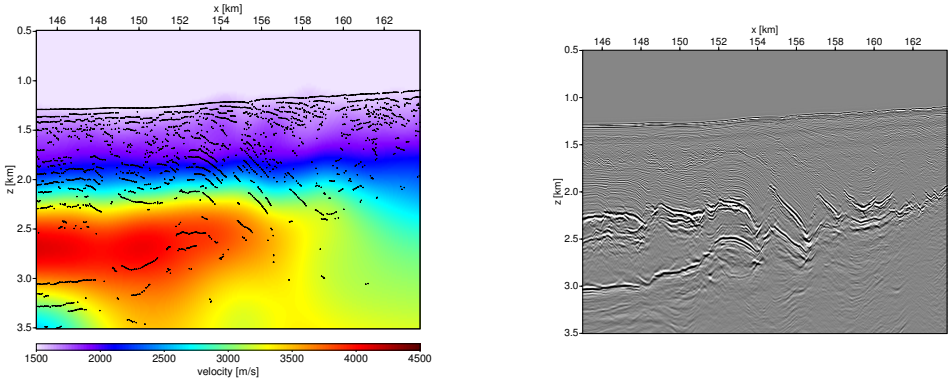

(a) NIP-wave tomography result.

(b) Corresponding migrated section.

Figure 8: The result of NIP-wave tomography. Overlaid over the velocity distribution the depth converted input data picks are imaged. On the right the corresponding prestack depth migration result.

In Fig 9 selected CIGs which are equally spaced over the whole profile part are imaged. The overburden and the M-reflections are flattened quite reasonable. Some down-bended residual move-out can be observed at the N-reflection for the reason mentioned above. Again an up-bending of the N-reflection can be recognized, indicating a too low average migration velocity. In the last three CIGs almost all reflections from 2000 m in depth show some residual move-out, which indicates that the regional traveltime approximation of NIP-wave tomography can hardly handle such a strong heterogeneous geological setting. Nevertheless the residual move-out is still in an order for a further model refinement.

Application of prestack stereotomography As for the first data set, to apply prestack stereotomography, the determination of the required input data had to precede the velocity model building. For this purpose, we performed the same steps. As in all other cases, the picking was followed by a first interactive quality control sequence. Since the same strong differences in the energy of the picks were observed in this example, the data were again split into three parts. In contrast to the other data example, the extracted input data already showed a good quality. Nevertheless, the same outlier removal based, on the global normalized misfit, was repeated. After this the total data was taken into the inversion scheme, starting with an initial model of $v(z) = 1500\ m/s + 0.5 s^{-1} z$ and a B-spline grid spacing of 500 m laterally and 500 m vertically. Again we added artificial picks in the water column to stabilize the inversion. Here, 10 localization steps preceded 20 joint inversion steps with a strong regularisation where an important decrease of the cost function occurred. The B-spline grid was then densified to 125 m vertically and further 11 joint inversion iteration with a loose regularization led to the best result.
Fig 10(a) presents the result obtained by prestack stereotomography. Again, the depth converted input data

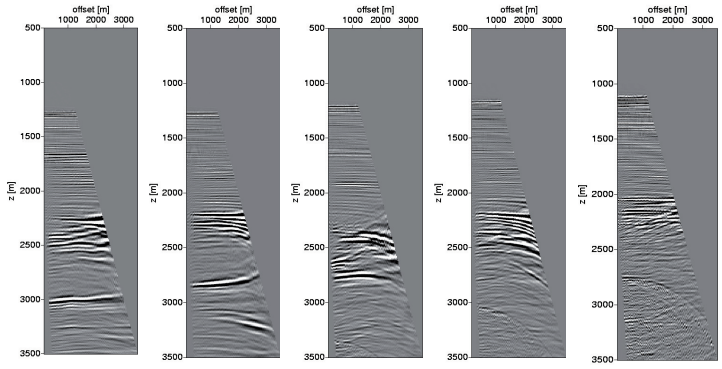

Figure 9: Selected CIGs from the prestack depth migrated NIP-wave tomographic result, equally spaced over the whole profile part.

picks are imaged overlaid on the velocity distribution. For this result the velocity distribution coincides with the assumed geological structures. All features observed in the stacked section can be recognized again. At a depth between 1100 m and 1300 m the location of the seafloor is characterized by a smooth increase in velocity and in the subjacent part a further rise to 2600 m/s matches the structures of the sedimentary overburden. In the following, the distinctive triangular pattern related to the salt rollers can be easily traced. Between 145 km and 156 km, velocities ranging up to 3700 m/s represent the evaporites, whereas in the neighboring part a slighter increase in velocity indicates their pinch-out. The input data coverage over the whole profile part is quite satisfying. Underneath the MU hardly any picks are visible, but again this was not the aim of this study.

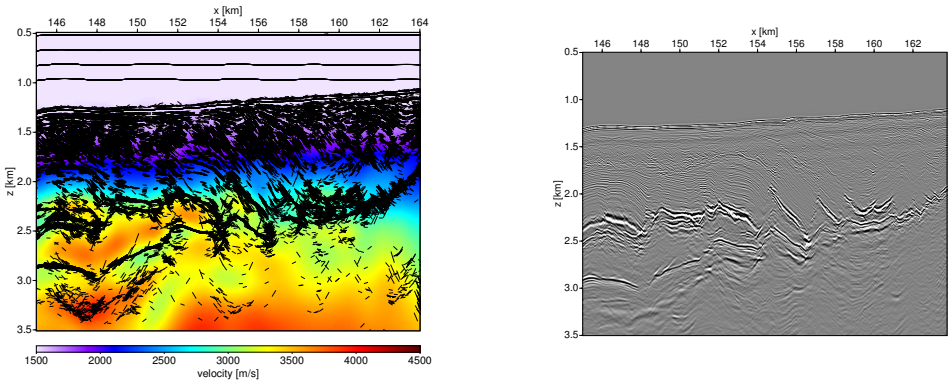

(a) Prestack stereotomography result.

(b) Corresponding migrated section.

Figure 10: The result of prestack stereotomography, The depth converted input data picks are plotted overlaid on the velocity model. On the right the corresponding prestack depth migration result.

Fig 10(b) represents the corresponding prestack depth migrated image. As before a good image quality was achieved and all assumed geological features are visible. The overburden and the top of salt reflection are locate at almost the same positions as before. Also the base of the evaporites is clearly mapped and reaches a maximum depth of about 3000 m. However, it shows distinctive interruptions and rough variations in depth can be observed, especially in the region of the salt rollers. Generally the image seems rougher and the structure are less continuous than in NIP-wave tomography.
The corresponding CIGs can are shown in Fig 11. They reflect the good image quality. The reflections form the overburden are mostly flattened. The top of salt reflection shows some negative move-out for

the same reason as in the first data example. Again the strong velocity contrast could not be described properly by the smooth model. The first two gathers in the region of the salt body, show some positive move-out, indicating a too low migration velocity. As a consequence, the depth of the N-reflection is not reliable determined. In the last three CIGs some slight down-bending for the strong reflections at 2000 m depth are observed, indicating a too high migration velocity. But generally the CIGs indicate a quite good result. Despite the good lateral resolution the result of prestack stereotomography is not completely data consistent, but serves as good starting model for a subsequent residual move-out analysis.

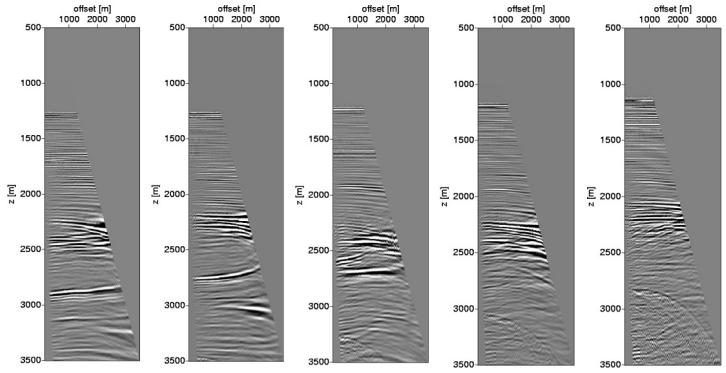

Figure 11: Selected CIGs equally spaced over the whole profile part.

Comparison of the results As shown by this real data example, both tomographic methods provide velocity models indicating major differences in the presence of strong lateral velocity contrasts. Whereas the velocity distribution found by prestack stereotomography (Fig 10(a)) resolves all important lateral velocity contrasts, the NIP-wave tomographic model (Fig 8(a)) features only smooth velocity variations and the distribution is more smeared over the section. Again this is linked to the three major theoretical differences of these methods, the traveltime approximations, the different order of B-splines, and the different regularizations of the inverse problem.

The data coverage was again better in prestack stereotomogarphy than in NIP-wave tomography. More picks could be obtained and complicated geological regions are better constrained, but the quality control and the preprocessing is much more challenging. This is due to the prestack data domain with its quite low signal-to-noise ratio. NIP-wave tomography has some disadvantages in the data coverage, but generally produces sufficient data to describe all important features.

The image quality of both prestack depth migration result is comparable, but some differences in the depth location and structural details occur. NIP-wave tomography produces smoother, horizontally more aligned events, while prestack stereotomography produces a rougher image. This is a direct consequence of the corresponding velocity distributions.

Despite the good quality of the related imaged sections, some residual move-out remains in the area of the salt body in both cases. The determination of a data consistent velocity model in terms of flat image gathers was not completely satisfactory in that region.

CONCLUSIONS

We have shown a comparison between two grid-based tomographic approaches for velocity model determination under equal initial conditions. The resulting models obtain partly different velocity distributions, but produce data consistent results in most areas in terms of flat common image gathers. The most striking differences are the resolution in the velocity model, the description of the model near fault zones, and the average velocities within the salt body. These three points are directly linked to theoretical differences of the methods compared in this paper. Additionally the individual evaporite sequences have been characterized by seismic velocities for the very first time. The derived sequence velocities of the distal evaporites

foster previously published interpretations of a vertical succession of alterning evaporite facies or intercalacted clastics.

The contrast in velocity resolution is directly linked to the underlying theory of both methods. Especially for the lateral resolution, the approximation of the traveltime curves reveals a major contrast. Prestack stereotomgraphy represents the traveltime curves by local slopes of locally coherent events. Only a part of the traveltime curve is described by its tangent (local approach) and therefore complex shaped traveltime curves may be accounted for. In NIP-wave tomography, over a large offset range, the traveltime curve is approximated hyperbolical, hence its a regional approach. Seismic events are assumed to be hyperbolic, otherwise they can not be inverted correctly. Offset information that deviates from the hyperbolic approximation is not considered during the inversion. This reduces the applicability of the method to moderate lateral inhomogeneous media (Klüver, 2006). Both resolutions, lateral and vertical, are influenced by the second major difference, that NIP-wave tomography uses one order higher B-splines than prestack stereotomography. This results in a velocity distribution which is smoother in the vertical and the lateral direction.
The differences in the description near fault zones are mainly related to two points. First, the input data for the tomographic approaches are determined in two different data domains. In prestack stereotomgraphy the input data is obtained in the prestack data domain by an automated picking tool, based on local slant stack panels. In contrast, in NIP-wave tomography the input data is picked in the poststack data domain using the results of the CRS stack. The input data determination in the prestack data domain is more challenging and the quality control has to be performed more carefully. But especially in regions with complex geological features yielding a decrease in coherency, the determination in the prestack data domain leads to a better data coverage. In NIP-wave tomography, the input data determination is simplified due to the high signal to noise ratio in the poststack data domain. However, in areas referring to fault systems, it is challenging to determine reliable attributes. The second reason for the differences occurring near fault systems is again the different representations of the traveltime curves mentioned above.
The third major inequality is the average velocity within the salt body. Here NIP-wave tomography produces higher average velocities than prestack stereotomography. On the one hand this fact might be related to the optimization of the processing for the comparison, that means that the obtained models are not necessary the best models that could be achieved with both approaches. On the other hand the different average velocities can be related to the different regularization of the approaches. Whereas in NIP-wave tomography the smoothest solution is explicitly sought by employing a minimum curvature constraint, in prestack stereotomography the model vector is required to have a bound on its norm. Depending on the regularisation weight, this may influence the velocity distributions also in terms of average velocities.

As seen before the major differences in the inversion results are directly linked to the formulation of both methods. The tomographic problems can be summarized as follows: in prestack stereotomography local slopes, their corresponding two-way traveltimes and spatial positions are used as input. In NIP-wave tomography the zero-offset traveltime, the spatial position, the horizontal slowness component and the second order spatial derivatives of the traveltime are used. In both methods, the input data is fitted in a least square sense to modeled data calculated by dynamic ray-tracing using a conjugate gradient like inversion scheme and a smooth velocity model is obtained that serves as a good starting model for further RMO analysis.

ACKNOWLEDGMENTS

The authors would like to thank:

- *TGS-NOPEC* for providing the data set
- *Gilles Lambaré* for the permission to use the prestack stereotomography code and the fruitful discussion
- The *Wave Inversion Technology consortium team Karlsruhe, Germany* for providing the NIP-wave tomography code
- The *Deutsche Forschungsgemeinschaft* (*DFG*), the *Integrated Ocean Drilling Project* Germany (*IODP*) and the *Wave Inversion Technology consortium* (*WIT*) for the financial support

REFERENCES

Bertoni, C. and Cartwright, J. (2006). Controls on the basinwide architecture of late Miocene (Messinian) Evaporites on the Levant margin (Eastern Mediterranean). *Sedimentary Geology*, 188-189:93–114.

Bertoni, C. and Cartwright, J. (2007). Major erosion a the end of the Messinian Salinity crisis: evidence from the Levant Basin/ Eastern Mediterrranean. *Basin Research*, 19:1–18.

Billette, F. and Lambaré, G. (1998). Velocity macro model estimation from seismic reflection data by stereotomography. *Geophys. J. Int.*, 135:671–690.

Clauzon, G., Suc, J., Gautier, F., Berger, A., and Loutre, M. (1996). Alternate interpretation of the messinian salinity crisis: controversy resolved? *Geology*, 24(4):363–366.

Duveneck, E. (2004). Velocity model estimation with data-driven wavefront attributes. *Geophysics*, 69:265–274.

Duveneck, E. and Hubral, P. (2002). Tomographic velocity model inversion using kinematic wave-field attributes. *SEG Technical Program Expanded Abstracts*, pages 862–865.

Garfunkel, Z., Arad, A., and Almagor, A. (1979). The Palmahim Disturbance and its regional setting. *Geological Survey of Israel Bulletin*, 72:56.

Gradmann, S., Hübscher, C., Ben-Avraham, Z., Gajewski, D., and Netzeband, G. (2005). Salt tectonics off northern israel. *Marine and Petroleum Geology*, 22:597–611.

Hertweck, T., Mann, J., and Klüver, T. (2005). Event-consistent smoothing in the context of the CRS stack method. *Journal of Seismic Exploration*, 14:197–215.

Hubral, P. and Krey, T. (1980). *Interval velocities from seismic reflection traveltime measurements*. Soc. Expl. Geophys., Tulsa.

Hübscher, C., Cartwright, J., Cypionka, H., De Lange, G., Robertson, A., Suc, J., and Urai, J. (2007). Global look at dalt giants. *EOS*, 88(16):177–179.

Hübscher, C. and Netzeband, G. (2007). Evolution of a young salt giant: The example of the Messinian evaporites in the Levante basin. *In: Wallner, M.; Lux, K.-H.; Minkley, W.; Hardy, Jr., H.R. (Eds.) The Mechanical behavior of Salt - Understanding of THMC Processes of Salt, Taylor and Francis Group, London*, pages 175–184.

Kearey, P. and Brooks, M. (1991). *An Introduction to Geophysical Exploration*. Blackwell Science, Oxford.

Klüver, T. (2006). Velocity model building using migration to residual time. *SEG Technical Program Expanded Abstracts*, pages 2022–2026.

Krijgsman, W., Hilgen, F., Raffi, I., Sierro, F., and Wilson, D. (1999). Chronology, causes and progression of the messinian salinity crisis. *Nature*, 400:652–655.

MacKay, S. and Abma, R. (1992). Imaging and velocity estimation with depth-focussing analysis. *Geophysics*, 57:1608–1622.

Mann, J. (2002). *Extensions and Applications of the Common-Reflection-Surface Stack Method*. Ph. D. thesis, University of Karlsruhe.

Mitchum, R., Vail, J., and Sangree, J. (1977). Seismic stratigraphy and global changes of sea-level, part 6: seismic stratigraphic interpretation procedure. *In: Seismic Stratigraphy - applications to Hydrocarbon exploration, American Association of Petroleum Geologists Memoirs*, 26:117–134.

Netzeband, G., Gohl, K., C., H., Ben-Avraham, Z., Dehghani, A., Gajewski, D., and Liersch, P. (2006a). The Levantine Basin - crustal structure and origin. *Tectonophysics*, 418:178–188.

Netzeband, G., Hübscher, C., and Gajewski, D. (2006b). The structural evolution of the Messinian Evaporites in the Levantine Basin. *Marine Geology*, 230:249–273.

Paige, C. C. and Saunders, M. A. (1982). Lsqr: An algorithm for sparse linear equations and sparse least squares. *ACM Trans. Math. Softw.*, 8:43–71.

Podvin, P. (2001). Automatic picking of locally coherent events for stereotomography. *Depth imaging annual report*, 1:315–326.

Ryan, B., Stanley, D., Hersey, J., Fahlquist, D., and Allan, T. (1970). The tectonics of the mediterranean sea. *In: Maxwell, A.E. (Ed.), The Sea, 4. Wiley, New York*, pages 387–491.